NuSTAR reveals the hidden nature of SS433

M. J. Middleton*, D. J. Walton, W. Alston, T. Dauser, S. Eikenberry, Y-F Jiang, A. C. Fabian, F. Fuerst, M. Brightman, H. Marshall, M. Parker, C. Pinto, F. A. Harrison, M. Bachetti, D. Altamirano, A. J. Bird, G. Perez, J. Miller-Jones, P. A. Charles, S. Boggs, F. Christensen, W. Craig, K. Forster, B. Grefenstette, C. Hailey, K. Madsen, D. Stern, W. Zhang

SS433 is the only Galactic binary system known to accrete at highly super-critical rates, analogous to tidal disruption events[1] and some high redshift quasars[2]. Probing the inner regions of SS433 in the X-rays is crucial to understanding the system yet has not been possible due to obscuration. *NuSTAR* observed SS433 in the hard X-ray band across multiple phases of its super-orbital precession period. Spectral-timing tools have allowed us to determine that the hard X-ray emission from the inner regions is scattered towards us by the walls of the wind-cone. By comparing to numerical models, we determine an intrinsic X-ray luminosity of $\gtrsim 1\times10^{38}$ erg/s and a face-on luminosity of $> 1\times10^{39}$ erg/s. A lag due to absorption by Fe XXV/XXVI in outflowing material travelling at least 0.14-0.29c strengthens the association with ultraluminous X-ray sources[3] and – in future - will allow us to map a super-critical outflow for the first time.

Discovered in 1977 from its bright H_α emission[4], SS433's defining characteristics are undoubtedly the helical motion of highly-collimated jets of plasma launched from its innermost regions and mass-loaded non-polar outflows[5,6] which together inflate the surrounding W50 supernova remnant. Knots in SS433's jet can be resolved at radio frequencies using very long baseline interferometry (VLBI) and indicate the presence of highly relativistic electrons[7], while the baryon content is revealed by emission lines ranging from H and He lines in the optical through to highly ionised Fe lines in the X-rays[8]. The Doppler shifts of the lines indicate motion with a period of ≈ 162 days, also seen in optical (HeII) emission lines originating from the non-polar wind[9]. Both the jets and winds carry a large kinetic luminosity, which requires extraction of energy via accretion onto a compact object. While the nature of the compact object in SS433 remains unknown (although dynamical arguments might imply the presence of a black hole[10]), the rate of mass transfer, as determined from optical lines[11,12], is thought to be ~1×10^{-4} $M_\odot$/year, orders of magnitude in-excess-of the Eddington limit for any plausible stellar remnant. Classical theory and radiation magneto-hydrodynamic (RMHD) simulations agree that such 'super-critical' rates of accretion will lead to a radiatively supported, large scale height (H/R ≈ 1 where H is the height of the disc at distance R from the compact object) accretion disc with powerful winds launched from the surface at mildly relativistic speeds[13,14]. The motion of the winds and jet are then explained by a periodic axial tilt of the giant secondary star and a slaved disc which precesses on the same timescale[15].

While super-critical systems are predicted to be extremely X-ray bright (with collimation by the wind leading to geometrical beaming for face-on inclinations[16]), SS433 is remarkably X-ray faint at only 10^{35} - 10^{36} erg/s (at an optical parallax distance of ≈ 4.6 kpc[17] determined using *GAIA*), orders of magnitude below the Eddington luminosity for a stellar remnant. This X-ray faintness implies that at no point during the system precession do we see down to the

* m.j.middleton@soton.ac.uk

central engine, consistent with a large scale-height inflow/wind and a mean inclination of 78 degrees to our line-of-sight[18]. Consequently, we have been unable to directly probe the nature of the extreme accretion onto the compact primary.

The X-ray continuum from the source below 20 keV is dominated by thermal Bremsstrahlung emission from the jet, and reveals the nature of the plasma from which the emission lines originate[8]. Above 20 keV there is a hard excess of emission, detected by both ESA's *Integral*[19] and NASA/JAXA's *Suzaku* satellite[20]. Models for the origin of this hard X-ray emission include a hotter component of the jet or reflection of the radiation emitted from within the wind-cone. The former would predict a single continuous spectral component with a range of temperatures, reflecting the increasing temperature of the jet plasma approaching the acceleration point, while the latter would appear as a spectral component distinct from that of the jet. In both situations, we might expect absorption by material associated with the outflowing wind along our line-of-sight. Determining the origin of the hard X-ray emission could reveal much about the inflow but requires obtaining the correct spectral model deconvolution. Time-averaged approaches often result in degenerate solutions (without prior assumptions for the underlying physics), however, applying time-resolved methods allows for a much 'cleaner' view.

NASA's *NuSTAR* X-ray satellite[21] has observed SS433 in the 3-79 keV band over several precessional phases. The observing dates and spectroscopic precessional phases - based on the well-established optical ephemerides[22] - are provided in Table 1. Even though the source is relatively X-ray faint, the high-quality spectra allow the changing emission properties of the system on long timescales to be studied in detail, and show the characteristic Fe XXV/XXVI emission lines moving with phase, and the hard excess becoming increasingly peaked above 20 keV with increasing flux. The source emission also varies on shorter, intra-observational timescales. From the highest signal-to-noise ratio datasets we extract the frequency-resolved, linearly correlated variability on these shorter timescales (across the 0.5-3.5 mHz frequency range – see Methods). The resulting covariance spectrum[23], shown in Figure 1, indicates the linearly correlated components in the spectrum and allows us to break the model degeneracies inherent in a time-averaged approach. By comparison to the time-averaged data, the covariance indicates that a two-component spectrum is required (see Figure one, lower panel). The fractional covariance (analogous to the fractional rms) at high energies is 20-30%, consistent with the largest amounts of variability typically detected in accreting sources[24], implying that the entire hard excess is formed from the linearly correlated component. The two-component nature of the covariance spectrum excludes the origin being a single intrinsically variable component (i.e. the jet) as this would be coherent (i.e. varying in lock-step) at all energies, and we can rule out an extrinsically variable higher energy component of the jet from inspection of the precession-phase-dependent changes in the hard and soft bands (see Methods).

The shape of the covariance spectrum shown in Figure 1 matches that of reflection from optically thick material, with a pronounced drop in flux consistent with the Fe K photoelectric edge and/or narrow absorption lines (appearing broad at these resolutions). To better understand the spectrum, we also extract frequency and energy-dependent time-lags between a band of interest and reference band (see Methods for details). As shown in Figure S1, these reveal the presence of a highly significant lag at 8-9 keV in several observations,

varying in magnitude with frequency. A lag across such a narrow energy range requires an atomic (rather than continuum) process. The lack of a structured lag spectrum resembling that of reflection implies that this is not associated with the Fe K edge, whilst the absence of multiple lag features would argue against it being associated with an emission line in the jet. Instead, the lag is most probably imprinted by transmission through outflowing, partially ionised gas with the magnitude (10s – 100s of seconds), providing an indication of the combined distance and density of the intervening material[25]. Given the energy of the lag feature (> 8 keV), the line is most likely Fe XXV or Fe XXVI, blue-shifted due to the line-of-sight velocity of the outflow, which should be depleted in Nickel relative to the jet[26]. We consider this the more likely explanation compared to absorption by Nickel, as, in the latter case, lines would be expected from both ionised species of Nickel and Iron, yet only one is present. Assuming the line is either Fe XXV or Fe XXVI, we find a range in the line-of-sight outflow velocity of 0.14-0.29c (which is potentially higher if we are not viewing along the direction of the outflow). This is consistent with outflows detected in the X-ray spectra of ultraluminous X-ray sources (ULXs[3]), also known to harbour super-critical accretion flows. Such line-of-sight velocities are in-excess-of those seen in the approaching jet ejecta at any precessional phase[18], further ruling out an origin in this dynamical component. The combination of identified reflection and absorption allows us to create the picture of SS433 shown in Figure 3 which leads to predictable changes as a function of precession.

The lack of a similar sized lag below the Fe K_α emission line energy indicates that the covariance spectrum is not heavily influenced by absorption by the same gas at lower energies, and so its shape must be close to that of the intrinsic reflected continuum. To determine the reflected flux as a function of precessional phase, we fit the time-averaged data with a model composed of reflection (based on the best-fitting, simple model for reflection to the covariance spectra as shown in Figure 1) and a model for thermal Bremsstrahlung at softer energies to account for emission from the X-ray bright jet. The resulting fits to the *NuSTAR* datasets are shown in Figure 3. We convert the reflected fluxes into inclination-dependent luminosities using the Doppler shift of the lines from the approaching jet, an assumed range in jet velocity (see Methods) and distance to SS433 of 4.6 kpc[17]. The observed luminosities can then be compared to simple theoretical models for reflection inside an optically thick wind-cone, and a lower limit on the intrinsic X-ray luminosity extrapolated. The theoretical models[27] subtend a large parameter space (in wind-cone opening angle and outflow velocity) and the 'correction factors' from observed to intrinsic luminosity diverge at very low-to-moderate inclinations. However, in all cases, the correction factor for the luminosity converges at the highest inclinations to > 1000. Based on our *observed* luminosity at the most edge-on phase (when we view the system at ≈90 degrees – Table 1), we infer an *intrinsic* X-ray luminosity for SS433 of $\gtrsim 10^{38}$ erg/s.

We plot some illustrative examples for wind-cone opening angles of 1 and 50 degrees and outflow velocities of 0c and 0.3c in Figure S3. While the model is relatively simple (for instance it assumes a perfectly conical geometry and achromatic scattering), the preference is for small opening angles, consistent with RMHD simulations[14] for accretion rates in excess of 1000 x the Eddington accretion rate, as inferred for SS433 from the optical lines[11,12]. While we only observe a faint apparent X-ray source, a *face-on* observer (e.g. in a local galaxy) would see an amplified luminosity as a consequence of collimation by the wind-cone[16]. For half-opening angles < 20 degrees (consistent with simulations of the source[28]), the X-ray luminosity would

appear in-excess-of 10^{39} erg/s, and SS433 would be classified as a ULX. While this has long been suspected[16,29], our direct constraint on the intrinsic X-ray luminosity confirms this assertion. The intrinsic radiative luminosity appears around or up to an order of magnitude smaller than the kinetic luminosity of the jet[30] (10^{38} - 10^{39} erg/s). The implication is that either there is an additional launching mechanism (other than radiation pressure) contributing to the mechanical jet power or some of the liberated radiation is advected along the jet. Once again, this implies that our derived intrinsic X-ray luminosity is a lower limit.

Similar extreme mass accretion rates as those seen in SS433 have been invoked in other objects, including tidal disruption events (TDEs)[1], and rapidly growing high redshift quasars[2]. However, neither of these are easy to study due to their inherently unpredictable appearance and rapidly diminishing brightness (TDEs), and distance (to both TDEs and quasars). We have demonstrated that in SS433 we can probe both the (otherwise unseen) super-critical inner regions and outflows through the application of established timing tools. Notably, with deep X-ray observations we will be able to model the phase-dependent lag and map the absorbing material in detail and thereby test theoretical models[13,14].

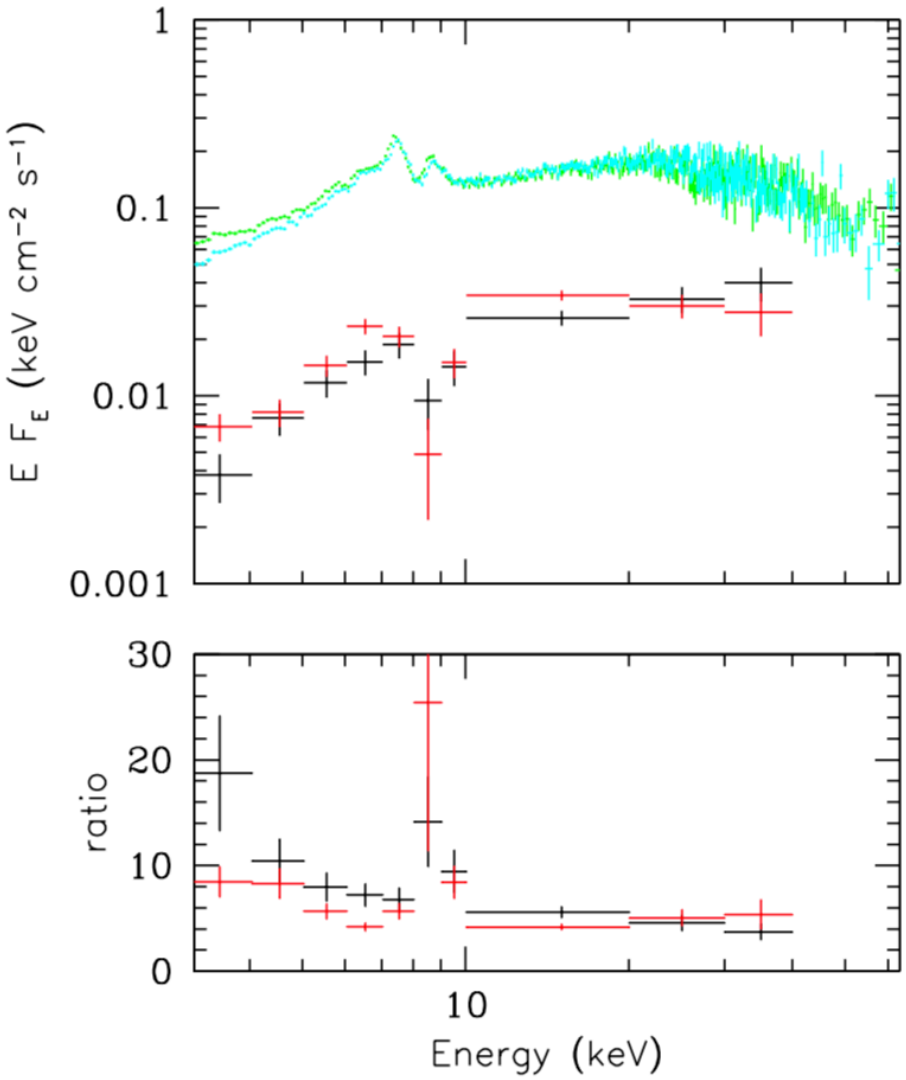

Figure 1: The covariance spectra of Obs 2 and Obs 7 (integrated from 0.5-3.5mHz) shown in red and black with the time-averaged data (green and cyan) for the FPMA only, both unfolded through a flat model (power-law of zero index and unity normalization). The ratio of the time-averaged data to the covariance is shown in the lower panel and is not consistent with a constant. This demands that the time-averaged spectrum is composed of multiple components.

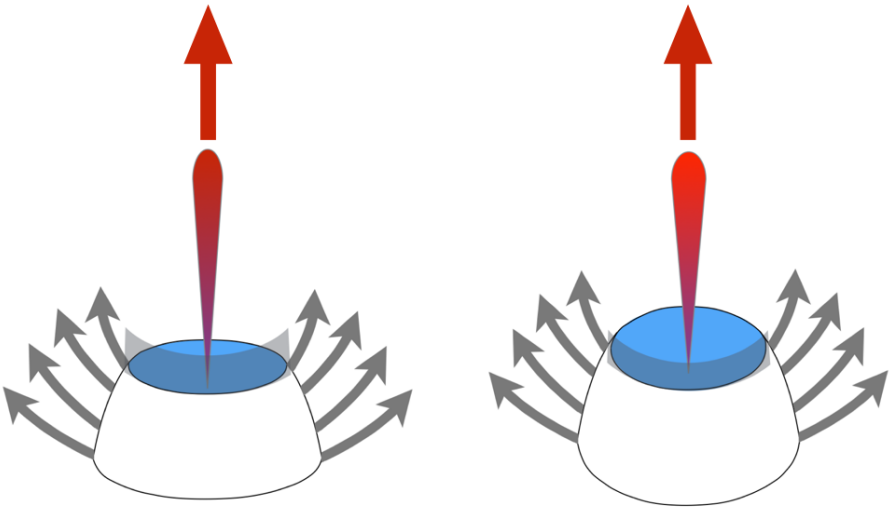

Figure 2: Schematic of SS433 based on our observations as a function of precessional phase. In both plots, the inflated disc launches an optically thick wind (grey arrows) which also presents a screen to the X-ray bright regions within the wind-cone (blue). As the system precesses to more face-on inclinations (left to right) the jet emission (red) at soft X-rays becomes brighter due to relativistic boosting whilst the reflected flux increases with the visible area of the open wind-cone[27].

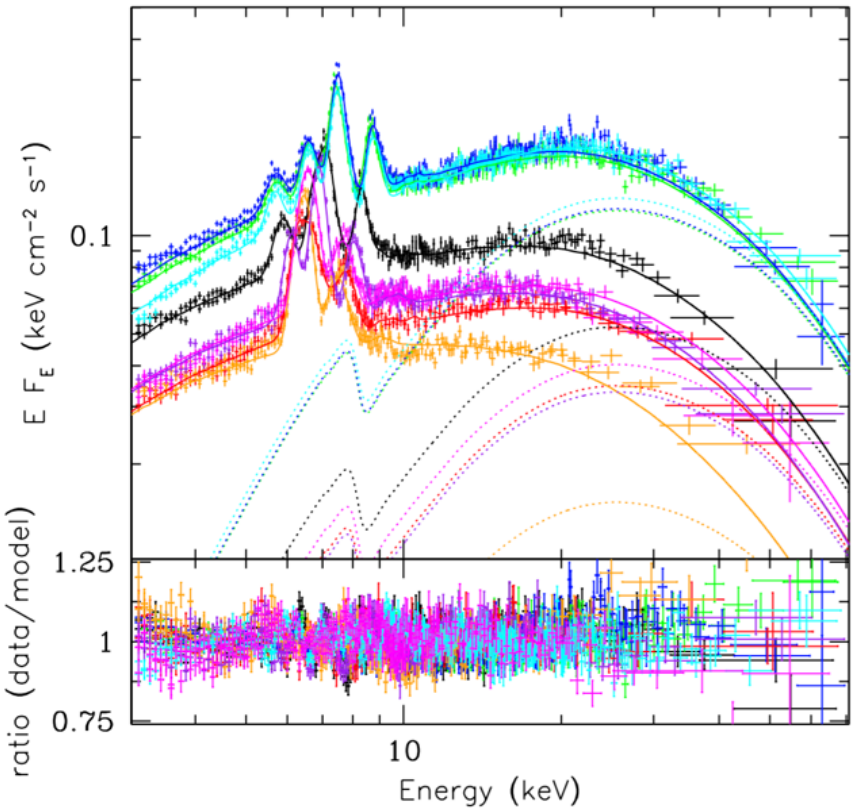

Figure 3: Time-averaged data for all observations (and both NuSTAR detectors) unfolded through the best-fitting model (see Methods and Table S2). The reflection component (pexrav) is highlighted as a dotted-line from which we determine the apparent luminosity as a function of inclination (derived from the Doppler shift of the approaching jet) as presented in Table 1. The lower panel shows the ratio of data to model.

Obs.	JD	T_{exp} (ks)	Ψ_{prec}	Ψ_{orb}	Θ (degs) v = 0.32c	Θ (degs) v = 0.26c	$L_{reflect}$ ($x10^{35}$ erg/s)
1	2456961	25	0.85	0.28	60.7	62.2	3.38 ± 0.03
2	2456974	29	0.93	0.28	53.8	53.6	7.67 ± 0.04
3	2456987	28	0.01	0.28	51.7	50.9	$7.77^{+0.05}_{-0.03}$
4	2457078	21	0.58	0.27	72.6	76.8	$2.23^{+0.03}_{-0.02}$
5	2457093	26	0.66	0.35	83.5	90.4	$0.98^{+0.03}_{-0.02}$
6	2457105	30	0.74	0.32	68.0	71.2	$2.13^{+0.03}_{-0.02}$
7	2457131	27	0.90	0.31	52.6	52.2	$8.38^{+0.05}_{-0.03}$
8	2457209	27	0.38	0.21	71.6	75.6	$2.59^{+0.02}_{-0.04}$

Table 1: Observational details for the *NuSTAR* campaign to observe SS433. Across the Table we report the date of the observations (in Julian days), exposure time, precessional and orbital phases (Ψ_{prec} and Ψ_{orb}, from the established ephemerides[9]), the inferred inclination of the wind-cone for two jet velocities and the observed luminosity in the reflected component ($L_{reflect}$) assuming a distance to the source from optical parallax of 4.6 kpc[17]. The latter are plotted versus inclination in Figure S3 from which an estimate of the intrinsic luminosity is obtained.

Methods

Model component (parameter | units)	Model = *tbabs*pexrav*	Model = *tbabs*gabs*pexrav*
Tbabs (n_H | x10^{22} cm^{-2})	< 3.59	< 4.59
pexrav (E_{fold} | keV)	$17.62^{+2.68}_{-5.68}$	> 15.92
pexrav ($\mathbf{\Gamma}$)	$1.74^{+0.27}_{-0.04}$	$2.10^{+0.32}_{-0.17}$
pexrav (z)	$-0.07^{+0.01}_{-0.02}$	$-0.12^{+0.04}_{-0.10}$
pexrav (Fe | solar abundance)	$3.53^{+1.15}_{-0.62}$	$1.51^{+0.58}_{-0.50}$
gabs (σ | keV)	--------	$0.43^{+0.14}_{-0.13}$
gabs (strength)	--------	$1.46^{+3.12}_{-0.52}$
χ^2 (d.o.f.)	29.62 (13)	17.56 (11)

Table S1: Spectral models and best-fitting parameters (with 1 sigma errors) from fitting to the covariance spectra shown in Figure 1.

Model = *constant*TBabs*gabs*gsmooth*(zgauss$_{1,app}$ + zgauss$_{2,app}$ + zgauss$_{1,rec}$ + zgauss$_{2,rec}$ + vvapec$_{app}$ + vvapec$_{rec}$ + pexrav)*	
Model component (parameter | units)	Value and 1σ errors
Tbabs (n_H | x10^{22} cm^{-2})	$2.39^{+0.03}_{-0.07}$
gsmooth (sigma | keV)	0.192 ± 0.002
gabs (strength)	$0.046^{+0.004}_{-0.002}$
zgauss$_1$ (E | keV)	6.739 ± 0.002
zgauss$_2$ (E | keV)	$7.845^{+0.002}_{-0.004}$
vvapec (kT | keV)	11.29 ± 0.03
vvapec (z_{app} – Obs1)	-0.055 ± 0.001
vvapec (z_{app} – Obs2)	-0.089 ± 0.001
vvapec (z_{app} – Obs3)	-0.098 ± 0.001
vvapec (z_{app} – Obs4)	0.009 ± 0.001
vvapec (z_{app} – Obs5)	0.073 ± 0.001
vvapec (z_{app} – Obs6)	-0.015 ± 0.001
vvapec (z_{app} – Obs7)	-0.094 ± 0.001
vvapec (z_{app} – Obs8)	0.004 ± 0.001
vvapec (Fe | solar abundance)	1.36 ± 0.01
vvapec (Ni | solar abundance)	$18.63^{+0.27}_{-0.18}$
pexrav (E_{fold} | keV)	$28.83^{+0.33}_{-0.21}$
pexrav ($\mathbf{\Gamma}$)	1.50 ± 0.01
χ^2 (d.o.f.)	7039 (4518)

Table S2: Spectral models and best-fitting parameters (with 1 sigma errors) from fits to the time-averaged spectra shown in Figure 3. The errors on the Doppler shifts have been rounded up to 0.001.

***NuStar* data extraction**

All observations obtained by *NuSTAR* were visually inspected for stray light with no contamination identified. We therefore extracted spectral and timing products using the *NuSTAR* pipeline, nupipeline[‡] v1.4.1 with 100 arcsecond source and background extraction regions and default SAA exclusion options. We further re-binned the spectral data to oversample the response by a factor 3 and such that each energy bin has a signal-to-noise ratio of 6. This resulted in sufficient counts/energy bin for chi-squared fitting.

Two additional observations to those reported in Table 1 were taken by *NuSTAR*, however, one of these only had data in a non-standard mode and was excluded while one showed unusual behaviour which will be discussed in a future work.

The cross spectrum

In this section we describe the timing analysis using multi-variate Fourier methods. From two evenly sampled time series x(t), y(t) we compute the cross-spectrum $C_{xy}(f) = X(f)*Y(f) = |X||Y|e^{i(\Phi y - \Phi x)}$ where * denotes the complex conjugate of the Fourier transforms X(f), Y(f), with amplitude and phase. We estimated cross-spectral products by first averaging the complex $C_{xy}(f)$ values over *m* non-overlapping segments of the time-series, and then averaging in geometrically spaced frequency bins (see [31] for more details on the use of the cross-spectrum).

From the argument of $C_{xy}(f)$ we obtain a phase shift (lag) $\Phi(f) = \arg \langle C_{xy}(f) \rangle$ which can be transformed into the corresponding time lag: $\tau(f) = \Phi(f) / 2\pi f$. This gives the (time-averaged) frequency-dependent time lag between any correlated variations in x(t) and y(t). Errors on $\tau(f)$ are estimated using standard formulae[31,32].

For a given Fourier frequency we can compute the time lag between a comparison energy band y(t) and a broad reference band x(t). The reference band is typically chosen to have a high signal-to-noise (S/N) so time delays between any correlated variations in bands with weaker S/N can be recovered. The comparison band is removed from the broad reference band when computing the lag between the two, in order to avoid any correlated noise between them[31]. A more positive lag value indicates the comparison-band lags the reference band.

We use a segment length of 1 ks so we have $m \gtrsim 25$ segments per observation, giving enough estimates for the errors to be Gaussian distributed. We use the 3-6 keV band as reference and summed FPMA and FPMB lightcurves. The power spectral density has significant power above the noise at low frequencies, such that we can explore the lags in the lowest three frequency bands: 0.5 – 1.5, 1.5 - 2.5 and 2.5 – 3.5 mHz. The lag versus energy spectra are shown in Figure S1; there is clearly a strong signature of a positive lag at most (if not all) frequencies in observations 1, 2, 3 and 7 in the 8-9 keV bin while the other observations show a noisier, more complicated behaviour. A lag over such a narrow energy range is only likely to result from emission/absorption processes in atomic transitions. Should the lag correspond

[‡] https://heasarc.gsfc.nasa.gov/lheasoft/ftools/caldb/help/nuproducts.html

to emission lines in the jet then we would expect to see lags of similar size at several energies but these are absent. A natural explanation would be a lag imprinted as a consequence of propagation of photons through an intervening outflowing medium (i.e. a wind), however, should this contain both Ni and Fe at abundances similar to that of the jet[30], then we should see multiple lines in the lag spectrum. The natural answer is that the outflow is far less abundant in Ni compared to the jets – as has been found by previous studies[26]. On the basis of this we determine that the likely association is with blue-shifted Fe XXV/XXVI resonance lines. The rest-frame energy of these absorption lines is 6.7 and 6.97 keV[33], implying an outflow velocity in the line-of-sight ranging from 0.14 to 0.29c, consistent with absorption lines detected in ULXs[3,34,35]. Given the jet velocity in the line-of-sight never reaches such values[19], this strengthens our assertion that the absorbing material is embedded in a less collimated (but similarly fast) outflow, i.e. the wind.

We can use the cross-spectrum to investigate the energy dependence of the variability (rather than only the lag between bands) across a range in Fourier frequencies. The covariance spectrum is analogous to an rms-spectrum[36] where the amplitude of C_{xy} (f) gives the coherence - the degree of linear correlation between x(t), y(t) as a function of Fourier frequency - which takes values in the range 0 to 1. We can use the coherence to obtain a Fourier frequency resolved covariance spectrum using the coherence and power spectra, $|X(f)|^2$ and $|Y(f)|^2$, following equation 13 of [31]. This provides the spectral shape of the components which are correlated with the reference band. We use the same segment averaging and reference band as with the time lags and obtain the covariance spectrum over the 0.5-3.5 mHz frequency range. The coherence between the two bands is > 0.4. As expected, the quality of the spectrum varies from observation to observation and is highest in observations 2 and 7 which we show in Figure 1 unfolded through a power-law of zero index and unity normalisation (to avoid bias inherent in unfolding the data through a model). In Figure 1 we plot the covariance along with the time-averaged data from the same observations and the ratio of the two. A constant fit to the ratio is statistically rejected in each case (null hypothesis probability < 0.05) – the linearly-correlated variable component in the spectrum cannot therefore account for the entire broad-band emission.

In order to explain the presence of a linearly-correlated variable component at high energies we must consider the physical options. Should the high-energy emission be associated with a hotter component of the jet, then any variability would have to become incoherent over a relatively small distance in order that the covariance is diminished by the time we observe the jet below 10 keV. Alternatively, we could be observing extrinsic variability imprinted by the crossing of optically thick clumps of wind[37,38,39] covering only the hot part of the jet. However, in order to imprint variability at energies > 20 keV requires extremely large (>10^{24} cm^{-2}), Compton thick columns of material at which point scattering would yield a broad Compton hump and the emergent spectrum would not be variable (as scattering dilutes variability unless the Compton thick wind itself is highly variable). We can also test whether a hot component of the jet – revealed to a greater or lesser degree by precession - could explain the long timescale variability in SS433 by studying the relative changes in the hard and soft bands as a function of precessional phase. In Figure S2 we plot the 3-15 keV (soft), 15-60 keV (hard) count rates and their hardness ratio (HR = hard/soft). For a constant velocity jet (emitting both at soft and hard energies), precession should result in equal amounts of Doppler boosting in both bands, resulting in a flat hardness ratio; as can be seen in the bottom

panel of Figure S2, this is clearly not the case. We can determine the minimum launch velocity the jet would require in order to match the observed boosting as a function of inclination. Using the standard Doppler boosting formula:

$$D = \delta^{3-\alpha} = \{\Gamma[1 - \beta\cos(\theta)]\}^{-1(3-\alpha)}$$

where α is the spectral index of the spectral component (across the energy range of interest), Γ is the jet bulk Lorentz factor ($1/\sqrt{1-(v/c)^2}$), β = v/c (where v is the jet velocity) and θ is the jet angle to the line-of-sight. Across the precession angle covered by our observations (≈ 50-90 degrees – Table 1) we see a change in boosting ($HR_{\theta1}$/ $HR_{\theta1}$) of at most a factor 2 (Figure S2). Thus, we have a relationship between HR, the cold (soft X-ray emitting) jet (subscript c) and hot (hard X-ray emitting) jet (subscript h) as a function of inclination (between θ_1 and θ_2):

$$\frac{HR_{\theta1}}{HR_{\theta2}} = \frac{D_{h1}S_h/D_{c1}S_c}{D_{h2}S_h/D_{c2}S_c} = \left[\frac{(\delta_h/\delta_c)_{\theta1}}{(\delta_h/\delta_c)_{\theta2}}\right]^{3-\alpha} = \left\{\frac{[1-\beta_c cos(\theta_1)]/\Gamma_{h1}[1-\beta_h cos(\theta_1)]}{[1-\beta_c\cos(\theta_2)]/\Gamma_{h2}[1-\beta_h\cos(\theta_2)]}\right\}^{3-\alpha}$$

where *S* denotes intrinsic (i.e. un-boosted) flux for each component. While the bulk Lorentz factors for the cold jet (Γ_c) have cancelled in the above formula (as the jet component emitting the Fe lines has a well-established, even if slightly variable, velocity[40]), those for the hot jet (Γ_h) do not, as the model we wish to test would predict that we see a different hot jet velocity at different inclinations to the system. We approximate this function by:

$$\beta_h = \frac{(v_{max} - v_c)\cos(\theta)}{c} + \beta_c$$

where v_{max} is the actual jet launch velocity and $v_c \approx 0.26c$ (i.e. $\beta_c \approx 0.26$). We can numerically solve for v_{max} knowing that at most θ_1 = 50 degrees, θ_2 = 90 degrees and assuming a reasonable lower limit on the spectral index of the thermal Bremsstrahlung emission in any broad energy band of α = -0.7. We find that, in order to match the observed dynamic range in hardness ratio, there is no acceptable solution for v_{max} (i.e. unphysically large velocities of >0.999c are required). The most viable explanation for the covariance spectra and relative changes in brightness as a function of precessional phase therefore appears to be a changing view of the reflected intrinsic flux by the precessing optically thick wind-cone, which we proceed to investigate in the following sections.

Covariance spectral fits

Based on the previous arguments, we fit the highest-quality covariance spectra (Obs 2 & 7) with an absorbed reflection component. We choose a simple model to fit the data in XSPEC (v12.8.2) of *tbabs*pexrav* where *pexrav* describes reflection from an incident cut-off powerlaw from neutral material[41] and *tbabs* accounts for absorption by neutral intervening material (with abundances from [42]) for which we set the lower limit to be the line-of-sight column in the direction of SS433[43] ($0.7\text{x}10^{22}$ cm^{-2}). We set the reflection scaling factor to be negative such that only the reflected emission is observed (i.e. the intrinsic continuum is absent). The resulting best-fit model parameters are presented in Table S1. We include a multiplicative *gabs* component with a centroid energy fixed at 8.5 keV (to be consistent with the center of the bin in which the lag is detected). The inclusion of this component implies a

significant change in $\Delta\chi^2$ (12 for 2 extra degrees of freedom). Although $\Delta\chi^2$ can often be misleading where the significance is not very large for an additive component[44], in this case, the lag spectra provide good reason to include such a line in our subsequent spectral fitting.

We note that the favoured Doppler shift of the reflection component implies motion *towards* the observer and at the 3-sigma level remains < 0. Although the reflected emission is affected by the combination of inclination via Doppler boosting (assuming at least mildly relativistic motion) and area of the reflector visible to the observer, we note that the inferred motion from our spectral fitting is degenerate with the ionisation state of the reflecting material. Indeed, it is highly probable – given the high accretion rates in this source and the radiation field which is obscured from view – that the material will be at least partially ionised rather than neutral as we have assumed for the sake of simplicity. We revisit this assumption in the following section.

Time-averaged spectral fits

Based on the fit to the covariance spectrum (above), we create a model for the time-averaged spectrum. The model is composed of Bremmstrahlung emission (*vvapec*) at soft (< 20 keV) energies to account for free-free emission from both the approaching and receding jet, with free abundances of Fe and Ni (the most relevant for our bandpass and known to be super-solar[30]) and Si, S, Ne and Mg set at 1.3 times solar[30]. We also tie the plasma temperature in the approaching and receding jets. We include two additional Doppler shifted Gaussian lines (*zgauss*) per jet to account for blends of lines not resolved by *NuSTAR* (with Doppler shifts tied to those in the Bremmstrahlung component and tied linewidths). We include reflection (*pexrav*, as described above) with free electron temperature and photon index tied across all observations. In doing so we are making the explicit assumption that the irradiating continuum does not change greatly with time. In addition, we tie the Fe abundance in the reflecting material to that in the Bremmstrahlung component.

We convolve the above model components with a Gaussian smoothing profile to account for turbulent motion (in this case we assume it is approximately the same in the jet and reflecting plasma). We also include a Gaussian absorption line (*gabs*) at 8.5 keV with the best-fitting line-width fixed to that from the fits to the covariance spectra (but normalisation free to vary) and absorption by neutral gas in the line-of-sight to SS433. Finally, we apply a constant offset between detectors to account for any differences in response (typically < 5%[45]). The final model in XSPEC is: *constant*TBabs*gabs*gsmooth*(zgauss$_1$ + zgauss$_2$ + zgauss$_3$ + zgauss$_4$ + vvapec$_1$ + vvapec$_2$ + pexrav).* We proceed to fit all spectral datasets simultaneously with plasma and electron temperatures, Gaussian smoothing, neutral column density, abundances, Gaussian emission line energies and absorption line strength tied across all observations (essentially allowing only the reflected flux and Doppler shifts to vary). The fit quality is statistically poor due to the extremely high quality nature of the data, the impact of multiple unresolved lines[8] and as a consequence of tying the continuum parameters across eight observations whereas in reality these may vary to some degree. However, in all cases the strongest line features and the continuum are well-described which is crucial for our analysis. The best-fitting model parameters of interest are provided in Table S2 with their approximate 1-sigma errors (with the exception of the Doppler shift for which the errors are very small and are rounded up to 0.001. We note that we also determine the abundance of

both Fe and Ni to be super-solar (with Ni being extremely so) as reported in previous campaigns[8].

From the Doppler shifts of the approaching jets (z_{app}, Table S2) we determine the inclination of our line-of-sight to the jet (θ), and therefore to the wind-cone. Accounting for transverse Doppler effects, we use the formula:

$$\theta = \cos^{-1}\left(\frac{1}{\beta}\left[2 - \left\{\frac{z_{app}+2}{\Gamma}\right\}\right]\right)$$

where β is the jet velocity in units of c - we assume a range of 0.26-0.32[40] - and Γ is the jet Lorentz factor ($1/\sqrt{1-\beta^2}$). We report the inferred inclinations in Table 1. We determine the integrated flux in the reflected emission (across 3-60 keV) by including a *cflux* convolution model component and derive the unabsorbed luminosity from the assumed distance to the source of 4.6 kpc[17] (and errors from the propagated uncertainty on the flux). These luminosities are provided in Table 1 and plotted versus the inferred mean inclination of the system (i.e. the mid-point of the values inferred from the jet velocity range) to our line-of-sight in Figure S3.

We note that the amount of fractional variability seen in the linearly correlated component at high energies is 20-30% which, by comparison with other accreting binaries (including both XRBs[25] and ULXs[38]), implies that the hard emission in SS433 is dominated by reflected emission. The resulting tying of parameters in the model is therefore necessary to ensure such a model deconvolution is obtained. In the case of the Doppler shifts this is not expected to introduce additional uncertainty as the lines are strong and well resolved, whilst the dominance of the *pexrav* component above 10-20 keV will minimise additional uncertainty on the reflected flux.

We note once again that our choice of a neutral reflector in our spectral modelling is a clear over-simplification and, in reality, the reflecting material is likely to have multiple ionisation zones. As we are simply determining the flux from integration of the model, our choice of a simple, neutral reflector rather than a more complex, partially ionised model, will not have any impact on the result.

A numerical approximation to the geometrical beaming effect has been obtained by performing a series of Monte-Carlo simulations of photons achromatically scattering a number of times until escaping from the optically thick wind-cone[27]. This allows an observed reflected luminosity as a function of inclination – such as we now have in the case of SS433 - to be mapped to a wind with a given opening angle, outflow velocity and intrinsic source luminosity (assumed to be located at the base of the wind-cone). In Figure S3 we overlay four of these theoretical models (for opening angles of 1 and 50 degrees and outflow velocities of 0c and 0.3c respectively) onto our data with the models scaled for ease of comparison but not fitted to the data. While a good fit is clearly not yet possible – unsurprising in light of the simplistic nature of the model - a small wind-cone opening angle does appear to be preferred. Importantly, even across a wide range of physical parameters for the wind-cone, the numerical models converge at inclinations above 80 degrees[27]. From this we can infer an approximate value for the correction to the observed luminosity at our highest inferred

inclination of > 1000. We note that the numerical models we are using assume achromatic scattering such that a comparison to observed luminosities assuming reflection from neutral material (as we have done), results in inferred luminosities which are a lower limit on the true luminosity. The implication is that the intrinsic luminosity is therefore ≥ $1x10^{38}$ erg/s which we note is around or above the Eddington limit for a neutron star. It is possible that the intrinsic luminosity is far higher - for instance, any advection along the jet will diminish the radiation escaping the wind-cone by reflection. Even assuming the lower limit on the inferred intrinsic luminosity, for opening angles of 20 degrees or less (as inferred for this source based on hydrodynamical simulations[28]) we would detect a face-on source of ≥ $1x10^{39}$ erg/s while for opening angles similar to that of the jet (< 1 degree[46]), the face-on luminosity would be > $1x10^{40}$ erg/s and SS433 would sit amongst the brightest ULXs presently known.

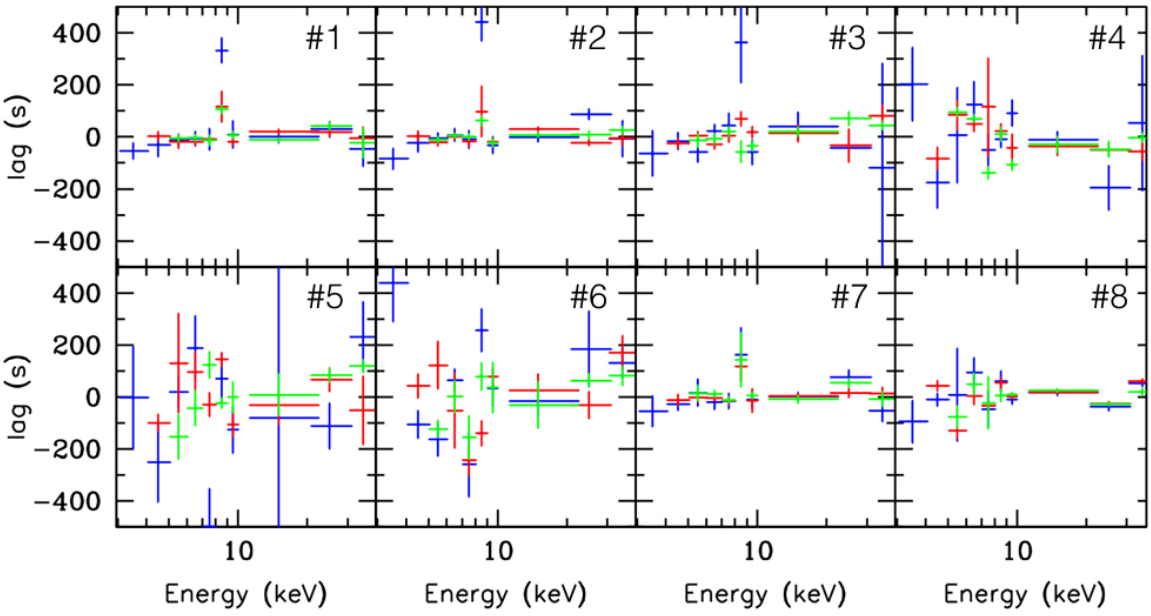

Figure S1: Energy-lag spectra for each observation of SS433 as a function of Fourier frequency where blue = 0.5-1.5 mHz, red = 1.5-2.5 mHz and green 2.5 – 3.5 mHz. There is clearly a significant lag in four observations (#1, #2, #3 and #7) in the 8-9 keV bin, indicating an atomic process. We infer that this is likely to be absorption of radiation by ionised species of Fe embedded in an outflowing medium, and the lag a consequence of propagation of photons through this material.

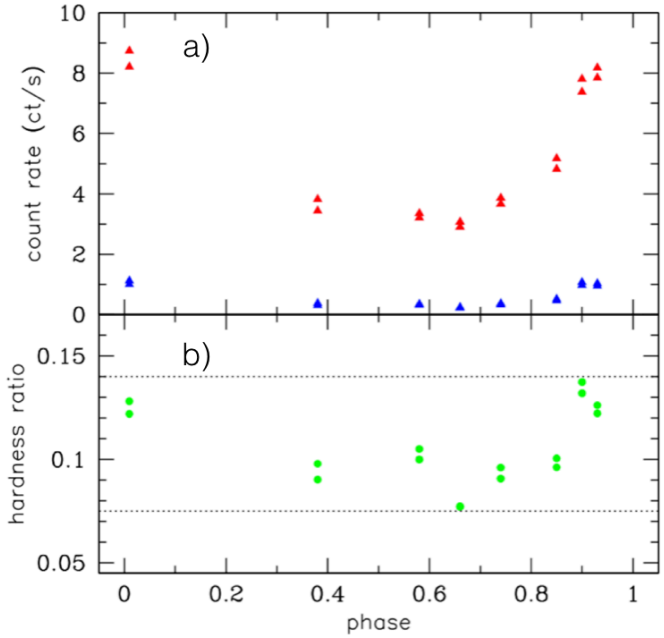

Figure S2: Panel a) soft (red: 3-15 keV) and hard (blue: 15-60 keV) lightcurves as a function of precessional phase (as determined from the ephemeris[9]. While the count rate in the soft band extends over a large dynamic range, that in the hard band extends across an even greater range (although the actual count rate itself is far smaller) as can be seen in panel b) where the ratio of hard/soft count rates is plotted and which subtends a range of 0.075 to 0.14 (i.e. a factor ≈2 in hardness ratio over the precession period). In all cases, the errorbars are smaller than the data-points.

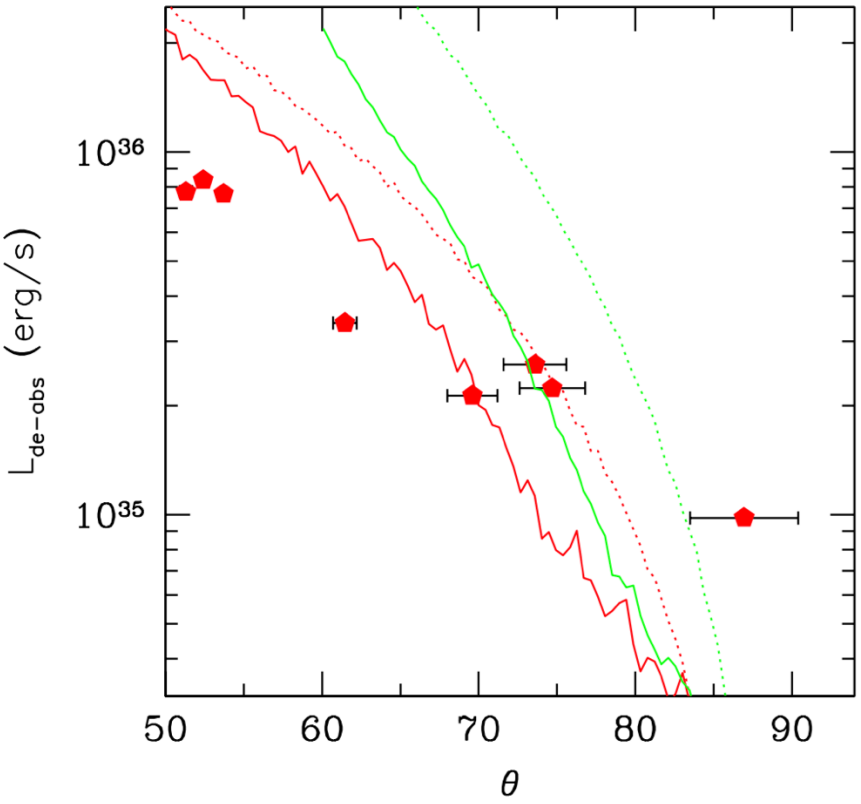

Figure S3: De-absorbed (3-60 keV) reflected luminosities for each observation as a function of inclination (as determined from the Doppler shift of the approaching jet). The errors on the luminosity are smaller than the data points and the error on the inclination results from the putative range in jet velocities. The red lines are theoretical curves for a 1 degree opening angle of a wind-cone, with material outflowing at 0c (solid line) and 0.3c (dotted line) and the green curves are the equivalent for an opening angle of 50 degrees. While the curves are not fitted to the data, they have been offset for the sake of clarity.

References:

[1] Rees, M. 'Dead quasars' in nearby galaxies? *Science*, **247**, 817-823 (1990).

[2] Volonteri M., Rees M.J. Rapid Growth of High-Redshift Black Holes, *ApJ*, **633**, 624-629 (2005).

[3] Pinto C., Middleton M.J., Fabian A.C. Resolved atomic lines reveal outflows in two ultraluminous X-ray sources. *Nature*, **533**, 64-67 (2016).

[4] Stephenson C.B., Sanduleak N. New H-alpha emission stars in the Milky Way. *ApJS*, **33**, 459-469 (1977)

[5] Fabian A.C., Rees M.J. SS 433 - A double jet in action, *MNRAS*, **187**, 13-16 (1979)

[6] Margon B., Ford H.C., Grandi S.A., Stone R.P.S. Enormous periodic Doppler shifts in SS 433, *ApJ*, **233**, 63-68 (1979)

[7] Vermeulen R.C., Schilizzi R.T., Icke V., Fejes I., Spencer R.E. Evolving radio structure of the binary star SS433 at a resolution of 15 MARC S. *Nature*, **328**, 309-313 (1987)

[8] Marshall H.L. *et al.* Multiwavelength Observations of the SS 433 Jets, *ApJ*, **775**, 75 (2013)

[9] Fabrika S.N., The Supercritical Accretion Disk of SS 433, *Ap&SS*, **252**, 439-450 (1997)

[10] Blundell K.M., Bowler M.G., Schmidtobreick L. SS 433: Observation of the Circumbinary Disk and Extraction of the System Mass. *ApJ*, **678**, L47 (2008)

[11] Shklovskii I.S. Mass Loss by SS433 and its Effect on the X-Ray and Radio Emission, *SvA*, **25**, 315 (1981)

[12] van den Heuvel E.P.J. SS 433, X-ray binaries and stellar evolution, *VA*, **25**, 95-108 (1981)

[13] Sadowski A., Narayan R., McKinney J.C., Tchekhovskoy A. Numerical simulations of super-critical black hole accretion flows in general relativity. *MNRAS*, **439**, 503-520 (2014)

[14] Jiang Y.-F., Stone J., Davis S.W. Super-Eddington Accretion Disks around Supermassive black Holes, *arXiv*, **arXiv:1709.02845** (2017)

[15] van den Heuvel E.P.J., Ostriker J.P., Petterson J.A. An early-type binary model for SS433. *A&A*, **81**, L7-10 (1980)

[16] King A.R., Davies M.B., Ward M.J., Fabbiano G., Elvis M. Ultraluminous X-Ray Sources in External Galaxies. *ApJ*, **552**, L109-112 (2001)

[17] Luri, X. *et al.* Gaia Data Release 2. Using Gaia parallaxes. *A&A*, **616**, A9 (2018)

[18] Eikenberry S.S., *et al.* Twenty Years of Timing SS 433. *ApJ*, **561**, 1027-1033 (2001)

[19] Cherepashchuk A.M. *et al*. INTEGRAL observations of SS433: system's parameters and nutation of supercritical accretion disc. *MNRAS*, **436**, 2004-2013 (2013)

[20] Kubota K. et al. Suzaku X-Ray and Optical Spectroscopic Observations of SS 433 in the 2006 April Multiwavelength Campaign. *PASJ*, **62**, 323-333 (2010)

[21] Harrison F.A., *et al*. The Nuclear Spectroscopic Telescope Array (NuSTAR) High-energy X-Ray Mission. *ApJ*, **770**, 103 (2013)

[22] Fabrika, S. The jets and supercritical accretion disk in SS433. *ASPRv*, **12**, 1-152 (2004)

[23] Wilkinson T., Uttley P. Accretion disc variability in the hard state of black hole X-ray binaries. *MNRAS*, **397**, 666-676 (2009)

[24] Munoz-Darias T., Motta S., Belloni T.M. Fast variability as a tracer of accretion regimes in black hole transients. *MNRAS*, **410**, 679 (2011)

[25] Silva C.V., Uttley P., Costantini E. Timing the warm absorber in NGC 4051. *A&A*, **596**, A79 (2016)

[26] Medvedev P.S., Khabibullin I.I., Sazonov S.Y., Churazov E.M., Tsygankov S.S. An Upper Limit on Nickel Overabundance in the Supercritical Accretion Disk Wind of SS 433 from X-ray Spectroscopy. *AstL*, **44**, 390-410 (2018)

[27] Dauser T., Middleton M., Wilms J. Modelling the light curves of ultraluminous X-ray sources as precession. *MNRAS*, **466**, 2236 (2017)

[28] Eggum G.E., Coroniti F.V., Katz J.I. Radiation hydrodynamic calculation of super-Eddington accretion disks. *ApJ*, **330**, 142-167 (1988)

[29] Khabibullin I., Sazonov S. Is SS 433 a misaligned ultraluminous X-ray source? Constraints from its reflected signal in the Galactic plane. *MNRAS*, **457**, 3963-3974 (2016)

[30] Marshall H.L., Canizares C.R., Schulz N.S. The High-Resolution X-Ray Spectrum of SS 433 Using the Chandra HETGS. *ApJ*, **564**, 941-952 (2002)

[31] Uttley P., Cackett E.M., Fabian A.C., Kara E., Wilkins D.R. X-ray reverberation around accreting black holes. *A&ARv*, **22**, 72 (2014)

[32] Vaughan B.A., Nowak M.A. X-Ray Variability Coherence: How to Compute It, What It Means, and How It Constrains Models of GX 339-4 and Cygnus X-1. *ApJ*, **474**, L43-46 (1997)

[33] Verner D.A., Verner E.M., Ferland G.J. Atomic Data for Permitted Resonance Lines of Atoms and Ions from H to Si, and S, Ar, Ca, and Fe. *ADNDT*, **64**, 1 (1996)

[34] Pinto C., *et al.* From ultraluminous X-ray sources to ultraluminous supersoft sources: NGC 55 ULX, the missing link. *MNRAS*, **468**, 2865-2883 (2017)

[35] Walton D.J., et al. An Iron K Component to the Ultrafast Outflow in NGC 1313 X-1. *ApJ*, **826**, L26-32 (2016)

[36] Revnivtsev M., Gilfanov M., Churazov E. The frequency resolved spectroscopy of CYG X-1: fast variability of the Fe K_α line. *A&A*, **347**, L23-26 (1999)

[37] Middleton M.J., Roberts T.P., Done C., Jackson F.E. Challenging times: a re-analysis of NGC 5408 X-1. *MNRAS*, **411**, 644-652 (2011)

[38] Middleton M.J., Heil L., Pintore F., Walton D.J., Roberts T.P. A spectral-timing model for ULXs in the supercritical regime. *MNRAS*, **447**, 3243-3263 (2015)

[39] Takeuchi S., Ohsuga K., Mineshige S. Clumpy Outflows from Supercritical Accretion Flow. *PASJ*, **65**, 88 (2013)

[40] Blundell K.M., Bowler M.G. Jet Velocity in SS 433: Its Anticorrelation with Precession-Cone Angle and Dependence on Orbital Phase. *ApJ*, **622**, L129-132 (2005)

[41] Magdziarz P., Zdziarski A. Angle-dependent Compton reflection of X-rays and gamma-rays. *MNRAS*, **273**, 837-848 (1995)

[42] Wilms J., Allen A., McCray R. On the Absorption of X-Rays in the Interstellar Medium. *ApJ*, **542**, 914-924 (2000)

[43] Dickey J. M., Lockman F.J. H I in the Galaxy. *ARA&A*, **28**, 215-261 (1990)

[44] Protassov R., van Dyk D.A., Connors A., Kashyap V.L., Siemiginowska A. Statistics, Handle with Care: Detecting Multiple Model Components with the Likelihood Ratio Test. *ApJ*, **571**, 545-559 (2002)

[45] Madsen K.K., *et al*. Calibration of the NuSTAR High-energy Focusing X-ray Telescope. *ApJS*, **220**, 8 (2015)

[46] Miller-Jones J.C.A., Fender R.P., Nakar E. Opening angles, Lorentz factors and confinement of X-ray binary jets. *MNRAS*, **367**, 1432-1440 (2006)